CENTRO AGRONOMICO TROPICAL DE INVESTIGACION Y ENSEÑANZA

PROGRAMA MANEJO INTEGRADO DE RECURSOS NATURALES

AREA DE MANEJO DE CUENCAS

PUBLICACIONES DEL PROYECTO RENARM/MANEJO DE CUENCAS

A SIMPLE METHOD TO STUDY AND CORRECT THE RADIOMETRIC EFFECTS DUE TO TOPOGRAPHY IN A RADAR IMAGE

Preparado por:
Grégoire Leclerc
Nathalie Beaulieu

CATIE, TURRIALBA
1994

electromagnetic pulses reach the surface. Geometric distortions can be removed in most cases by considering the sensor-surface geometry, requiring a knowledge of the trajectory and look-angle of the sensor and the availability of a Digital Elevation Model (DEM).

Now some commercial image processing packages offer the possibility of the precise orthorectification of radar images using a DEM, including the radar modules of EASI/ PACE (PCI, Inc.), EARTHVIEW (Atlantis Scientific Systems Group, Inc.) and SRIT (Toutin, 1992). For the radiometric correction of topographic effects, specific programs have been developed in research centers and universities (Teillet *et al*, 1985; Hinse *et al*, 1989, Bayer *et al*, 1986, Wivell *et al*, 1992), but to date we do not know of commercially available packages offering this capacity. On the other hand, within the radar analysis package of PCI or EARTHVIEW, a simulated radar image can be constructd from an orthoimage and a DEM (PCI, 1992, EARTHVIEW, 1993). This image can be used to carry out a radiometric normalization, in the same manner that an artificially illuminated DEM can be used to correct an image in the optical domain. Using this method, however, there is no control over the illumination parameters. PCI's SARSIM1 and SARSIM2 programs, for instance, simulate a SAR image using an approximation of the $1/\sin(\theta_r)$ to account for the slant range scale compression, with θ_r being the local incidence angle in the range direction (Guindon and Adair, 1992).

The objective of this paper is to introduce a simple solution to acount for the radiometric effects related to topography on a radar image. It explains how any orthorectification software can be used to generate an image of the incidence angle, which in turn is combined with a DEM to correct the dependence of the radar return on topography.

2. PROPOSED METHODOLOGY.

Because it is not registered to the topographical information, a slant-range image cannot be directly submitted to a correction of the radiometric effects of the topography. The image first has to be georeferenced and the geometric distortions corrected, preferably accounting for topography if it is significant. During this process, the image is rotated and its pixels shifted in the range direction, according to the severity of the topography. The calculation of the incidence angle becomes a somewhat complicated process, requiring the calculation of the distance between the sensor and a pixel to the ground, as a function of the trajectory of the platform and of the geographical coordinates. Indeed, the incidence angle is much more easily related to the slant range in the raw image than to the geographic position of a pixel in the corrected image.

The method presented here involves three steps: (a) a strategy for the calculation of the incidence angle with respect to the vertical at the terrain surface; (b) the calculation of the local incidence angle in both range and azimuth directions, which depends on the topography and on the flight and look directions; (c) the radiometric correction which involves the application of a gain factor that varies with the local incidence angle.

The central idea of our method is to create a synthetic image in slant range projection having the same dimension as the radar image being studied, in which the Digital Number (*DN*) of each pixel *(i, j)* is proportional to the slant range distance *SLR(i, j)* which is a linear function of the column number *i*. The resulting image has a gradation of intensity increasing linearly from the near range to the far range. This image is orthorectified with the same parameters as were used to rectify the radar image, resulting in the creation of a georeferenced synthetic image in which, for each pixel in ground range coordinates *(x,y)*, the slant range *SLR(x,y)* of this pixel can be readily computed from the *DN* (figure 1). This new image is the basis for the calculation of other parameters needed for the radiometric analysis.

a) Computing of the incidence angle

With the knowledge of the viewing geometry, one can calculate the *incidence angle with respect to the vertical* at the surface of the terrain $\theta_i(x,y)$ for each pixel. A comprehensive description of the viewing geometry of ERS-1 can be found in Laur, 1992. In the case of a sensor of constant altitude ALTI. the viewing geometry is simple, as seen in figure 2a. In this case $\theta_i(x,y)$ is calculated from the slant range *SLR(x,y)* and the terrain elevation *H(x,y)* at pixel *(x,y)*, by means of Equation 1:

$$\theta_i(x,y) = \cos^{-1}\left(\frac{ALTI - H(x,y)}{SLR(x,y)}\right) \qquad (1)$$

The image of θ_i (figure 3a) is later used to compute the local incidence angle in step b), and is in itself essential for the study of the backscattering by vertical elements such as trees and certain crops. $\theta_i(x,y)$ computed for an arbitrary horizontal surface at a reference elevation, is used in the normalization of the image with respect to a flat surface, as described in section 2 d).

b) Computing of the local incidence angle.

To simplify the notation, we will consider the range and azimuth axes separately, and compute the corresponding components of the local incidence angle (see figure 2). We first have to compute the terrain slope in these two directions, which is achieved through the use of programs included in most raster Geographical Information Systems (GIS) and image processing software. These allow to calculate the slope *S(x,y)* with respect to a horizontal plane and the aspect *A(x,y)* of the terrain with respect to the geographical north.

In the range direction the local incidence angle $\theta_r(x,y)$ (figure 3b) is the sum of the terrain slope projected along the range axis $S_r(x,y)$, and the incidence angle $\theta_i(x,y)$:

$$\theta_r(x,y) = S_r(x,y) + \theta_i(x,y) \quad (2)$$

where $S_r(x,y)$ is calculated from the slope and aspect of the terrain, and sensor's heading (*HEAD*). For right- looking images:

$$S_r(x,y) = S(x,y) \cdot \cos(A(x,y) - HEAD + 270) \quad (3)$$

where *HEAD* and $\theta_i(x,y)$ are expressed in degrees. The image of θ_r can be thresholded to build *approximate* shadow and layover masks: areas with θ_r greater that 90° will be shadow areas (although this does not account for casted shadows), while negative θ_r lie in layover areas (some layovered areas have however positive θ_r).

In the azimuth direction, the local incidence angle $\theta_a(x,y)$ (figure 3c) is simply given by the terrain slope projected along the azimuth axis:

$$\theta_a(x,y) = S(x,y) \cdot \cos(A(x,y) - HEAD) \quad (4)$$

The parameters $\theta_i(x,y)$, $\theta_r(x,y)$, and $\theta_a(x,y)$ form distinct layers of a GIS, which can be used to make a semi-empirical analysis of the radar backscattering.

c) Radiometric Correction.

At this point it is necessary to choose a backscattering model that will allow us to perform a radiometric normalization. One model may be given by the fit of an arbitrary function to the image data, with $\theta_i(x,y)$, $\theta_r(x,y)$, and $\theta_a(x,y)$ as independent variables (Itten and Meye, 1993). One may otherwise assume a specific angular dependence of the scattering function (Teillet *et al*, 1985, Wivell *et al*, 1992, Bayer *et al*, 1991). We elected to consider *lambertian scattering* (equal diffusion in all directions and no absorption), and to correct the image with a synthetic image of lambertian surfaces. This allows the analysis of the *deviation* with respect to the lambertian scattering, which offers valuable insights on the type of scattering involved. It highlights the angular behavior of both the specular scattering (elastic scattering) and absorption (inelastic scattering), both of which are characteristic of a particular target.

Let us examine the energetics involved in this procedure. The incident irradiance (incident flux per unit area) that reaches an inclined surface is equal to the irradiance that would have received a surface perpendicular to the incident wavefront, multiplied by $[\cos(\theta_r) \cdot \cos(\theta_a)]$ which is the projection of the unit surface on the wavefront. With the wavefront being dispersed equally in all directions (lambertian surface), only the projection of the terrain visible from the antenna will be measured, implying another $[\cos(\theta_r) \cdot \cos(\theta_a)]$. The backscattering coefficient σ^0 has been defined by Elachi (1987) as the ratio of the

energy backscattered by a surface to the energy that would have been received if the surface was lambertian and facing the wavefront. The backscattering coefficient of a lambertian surface which direction vector is parallel to the look direction is therefore equal to one, which implies that the backscattering coefficient of a lambertian inclined surface σ_l^0 is given by[1]:

$$\sigma_l^0 = \cos^2(\theta_r(x,y)) \cdot \cos^2(\theta_a(x,y)) \tag{5}$$

In the airborne images of the X-C SLAR of the Canadian Center of Remote Sensing (CCRS) as well as in ERS-1 images, the *DN* is related but not proportional to the square root of the backscattering coefficient. First of all, system-dependent gain factors such as antena pattern, STC gain, noise power, etc... are affecting the *DN*. In order to compute σ^0 using digital images we also have to compensate for a variable pixel size in the ground-range projection: in the slant-range image, the *DN* of a pixel corresponds to an area on the ground which is which $[\sin(\theta_r) \cdot \cos(\theta_a)]$ times larger than the slant range pixel; the theoretical *DN*, in absence of noise and for lambertian scattering is therefore given by Equation 6. It should be pointed out that areas with θ_r greater than 90° are shade areas, so that any signal in these areas can be atributed to noise.

$$DN_l^2(x,y) = \frac{k(x,y) \cdot \sigma_l^0(x,y)}{\sin(\theta_r(x,y)) \cdot \cos(\theta_a(x,y))} \qquad \theta_r, \theta_a < 90°$$

$$DN_l^2(x,y) = 0 \qquad \theta_r \geq 90° \tag{6}$$

where $k(x,y)$ is the proportionality factor which takes into acount the system-dependent factors. Developping σ_l^0, we obtain:

$$DN_l^2(x,y) = k(x,y) \cdot \frac{\cos^2(\theta_r(x,y))}{\sin(\theta_r(x,y))} \cdot \cos(\theta_a(x,y)) \qquad \theta_r, \theta_a < 90°$$

$$DN_l^2(x,y) = 0 \qquad \theta_r \geq 90° \tag{7}$$

Elimination of topographic effects.

SAR systems are calibrated with respect to ground at a reference elevation H_{ref} (which

[1] Many authors suppose a $\cos(\theta_i)$ dependence for σ^0 of the amazonian rain forest. A constant γ ($\gamma = \sigma^0/\cos(\theta_i)$), although not consistent with isotropic scattering, seem to better describe the inelastic and elastic angular dependence of the scattering in C-VV over tropical rain forest, for incidence angles between 20° and 60°.

correspond to the GEM6 ellipsoid in the case of ERS-1 images), and any surface at an elevation other than H_{ref} will be contain some radiometric distortion since the incidence angle at a given (x,y) position varies with the elevation. Our interest here is to develop a correction for the topographic effcts only, leaving the image untouched if the corresponding terrain is flat and at an elevation H_{ref}; the correction factor will be different from one in cases of uneven topography and when the surface lies at an elevation different than H_{ref}. This correction factor can be calculated as follows. For a flat terrain at an elevation H_{ref}, equation 7 becomes:

$$DN_l^2(x,y)\,|_{H=H_{ref}} = k(x,y)\cdot\frac{\sigma_l^0(x,y)|_{H_{ref}}}{\sin\left(\theta_i(x,y)\,|_{H_{ref}}\right)} \qquad (8)$$

$$= k(x,y)\cdot\frac{\cos^2\left(\theta_i(x,y)\,|_{H_{ref}}\right)}{\sin\left(\theta_i(x,y)\,|_{H_{ref}}\right)}$$

An image of $\frac{DN(x,y)}{DN(xy)|_{H_{ref}}}$ will have the required qualities, being equal to one if the terrain is flat and at the reference elevation. By doing this, we also eliminate $k(x,y)$, the system dependent calibration parameter. The image with topographic effects removed, $DN_{cor}(x,y)$, is therefore obtained by normalizing by the image of $\frac{DN(x,y)}{DN(xy)|_{H_{ref}}}$. Explicitely, we find:

$$DN_{cor}(x,y) = \left(\frac{DN_l^2(x,y)|_{H_{ref}}}{DN_l^2(x,y)}\cdot\left[DN^2(x,y) - DN_n^2(x,y)\right]\right)^{1/2}$$

$$= \left(\frac{\cos^2\left(\theta_i(x,y)\,|_{H_{ref}}\right)}{\sin\left(\theta_i(x,y)\,|_{H_{ref}}\right)}\cdot\frac{\sin(\theta_r(x,y))}{\cos(\theta_a(x,y))\cdot\cos^2(\theta_r(x,y))}\cdot\left[DN^2(x,y) - DN_n^2(x,y)\right]\right)^{1/2} \qquad (9)$$

$$\theta_r, \theta_a < 90°$$

$$DN_{cor}(x,y) = 0 \qquad \theta_r \geq 90°$$

where $DN_n^2(x,y)$ is the range-dependant noise power (it can be assumed negligible or estimated by using shadow areas in the image). This correction diverges as θ_r and θ_a get

closer to 90°, as can be seen in figure 4. The divergence rate is however much greater in the range direction than in the azimuth direction.

Antenna pattern correction and absolute calibration.

An image corrected using equation 9 will be substantially flattened radiometrically, and therefore more suitable for an empirical antenna-pattern and noise power correction. Since system-dependent radiometric distortions (such as antenna pattern, STC gain modulation, noise power) are functions of the slant range principally, we can use the layer *SLR(x,y)* as the independent variable. This image can also be calibrated when calibration parameters are known, using:

$$DN_{cor}^{cal}(x,y) = \frac{1}{k(x,y)} \cdot DN_{cor}(x,y) \tag{10}$$

We can relate equation 10 to other work done on the radiometric calibration of SAR images. A factor $1/\sin(\theta_i)$ appears explicitely in the radar equation for RAR and SAR (Ulaby and Dobson, 1989). The factor $\sin(\theta_i \mid_{Href})$ of Equation 8 is therefore found in the definition of $F'_{cal}(SLR)$, the slant-range dependent calibration factor for South American Radar EXperiment (SAREX) data (Hawkins and Teany, 1994), as well as in the definition of $K(\alpha)$ ($\alpha \equiv \theta_i \mid_{Href}$) for ERS-1 image calibration (Laur, 1992). These calibration parameters are given for flat terrain at a reference elevation H_{ref}, and can easily be related to $k(x,y)$, based on equation 8. For SAREX data, we obtain:

$$k(x,y) = \frac{\sin\left(\theta_i(x,y) \mid_{H_{ref}}\right)}{F_{cal}'(x,y)} \tag{11}$$

and for ERS-1 data:

$$k(x,y) = K\left(\theta_i(x,y) \mid_{H_{ref}}\right) \cdot \sin\left(\theta_i(x,y) \mid_{H_{ref}}\right) \tag{12}$$

3. RESULTS

We have applied our method to C-SAR slant-range image subsets of the Juan Viñas area, Costa Rica. The flight lines 8.2 and 8.3 were part of the outcomes from *Proyecto Radar Costa Rica Canada* and a complement to the SAREX mission in Latin America (Ahern *et al*, 1994, Wooding *et al*, 1994). They were aquired on April 27th, 1992 in C band, narrow-mode, HH and VV polarizations, with the X-C SLAR system aboard the Convair 580 of the Canadian Center of Remote Sensing. These images have a resolution of 6mx6m and a pixel size of 4m in slant range and 4.31m in azimuth. They cover the study area with different

depression angles and opposite look-directions. Field work was conducted simultaneously with the acquisition providing an extensive database and a collection of hand-held 35mm photos taken from a small airplane and from surrounding lookouts. These proved essential for our analysis of the radar backscattering.

For the geometric correction of the radar images, we used FLIGHT and STGBIG, of EASI/PACE's radar module, permiting the production of orthoimages with ± 2m (rms) precision in X and Y, with 23 ground control points taken from road intersections and field boundaries. A nearest neighbour resampling was applied to preserve the radiometry of the original image. A DEM was interpolated from the contour lines of 1:10000 scale topographic maps (based on 1989 airphotos). The DEM was interpolated according to a 2x2m grid utilizing INTERCON, of the raster GIS IDRISI; a 5×5 median filter was then applied to it, followed by a contraction to a 4mx4m pixel, and subsequent 5x5 median filtering. This procedure resulted in a DEM with an estimated precision of ± 1m in altitude. In the georeferenced radar image of the study zone corresponding to flight line 8.3 (figure 5a), one can percieve that the area presents a lightly undulated relief that is cut vertically by the canyon of Quebrada Honda. It is covered by sugarcane in mild slopes, and by coffee, forest, plantain banana and vegetable crops in steep slopes.

For these test sites a correction for topography only was expected to give good results since SAREX data was intended for visual interpretation principally, implying that the data had to present an even radiometry in level terrain. On figure 4b is shown the image in figure 4a that has been corrected using Equation 9, taking $H_{ref} = 0$ (figure 4b). We can see that the image's radiometry has been substantially flattened and that departure from lambertian scattering becomes easy to track, especially at high ($>70°$) local incidence angles. As pointed out by Elachi (1987) the radar return signal brings more information on the small-scale structure for high θ_r, while for low θ_r it provides information on the surface slope distribution; this is evidenced here as the slope facing the radar in the Quebrada Honda canyon, which presents values of θ_r close to zero, has been almost perfectly corrected. On these slopes we can now distinguish forest and plantain banana plantations from coffee plantations.

The area shown by the arrow is a moist bare soil field recently plowed with the heavy plough, which presented a very rough surface (>25cm RMS). In the uncorrected image, we might have atributed this unusually high return to topographic effects such as those appearing in the surroundings. The radiometric correction removes the ambiguity, as the field preserves its high return while the surrounding bright areas disappear.

θ_i, θ_r, and θ_a images provide useful information for the study of radar scattering on specific targets. For example, we found that mature sugar cane fields appear suddenly dark (raw DN lower than DN_l) for values of θ_r greater than 77°. Maybe the leaves of the plants start to act as specular reflectors, or the fields start to absorb the incident wavefront at this particular incident angle. Coffee seemed to behave differently, with the DN being higher than expected from a lambertian scatterer, suggesting the presence of corner reflectors in the

coffee bush structure.

On the other hand, trees and buildings now show up as very bright spots since they act as corner reflectors and not as lambertian targets. This reduces somehow the visual quality of the images but allows an easier detection of such components.

4. CONCLUSIONS

We have presented an effective method to study and correct topographic effects in SAR images. The method is relatively simple and easy to implement, and does not require sophisticated software or code-level programming. In fact any rectification software (with affine or radar-specific algorithms) can be used to generate a georeferenced image of the slant range. This image, together with the DEM, is then used to generate images of the local incidence angle along the range and azimut directions. Empiric or semi-empiric scattering model can then be applied and tested against the SAR image.

In the area of Juan Viñas, Costa Rica, high-resolution C-SAR image susbsets have been normalized with a synthetic image assuming lambertian scattering. The removal of topographic features appeared excellent for local incidence angles up to 70°, while for higher local incidence angles small-scale structure have pronounced effects in the radar return and were not corrected.

For this study we counted with a high precision DEM, generated from 1:10000 scale topographic maps, and were able to achieve a very good registration of the SAR image. This allowed to obtain a good radiometric correction. If the image is not well registered to the DEM, artifacts appear after normalization that reduce greatly the utility of the process. With a DEM made from 1:50000 scale maps, intensity variations due to meso-relief cannot be taken into acount, and therefore the normalized image will still present a granular apearance. This effect can be atenuated by matching the image resolution to the DEM resolution.

AKNOWLEDGEMENTS.

We would like to thank Alexander Salas, CATIE technician in charge of the digitizing. Special thanks to Frank Ahern, from CCRS, who brough us an excellent technical support and useful comments. PCI, Inc. lent us full versions of EASI/PACE, without which it would have been very difficult and lenghtly to conduct this study. Thanks also to David Williams for revising the manuscript. The Proyecto Radar Costa Rica/Canada, coordinated by the Instituto Geografico Nacional de Costa Rica (IGN), provided the images as well as a platform for interesting scientific exchanges. This study was financed by the International Development Research Center (IDRC) of Canada, the National Research Council of Canada, the SYNERGIE program of the Fonds de Developpement Technologique du Quebec, and

the United States Agency for International Development (USAID).

REFERENCES

TEILLET, P. M., GUINDON, B., MEUNIER, J. -F., and GOODENOUGH, D. G., 1985. "Slope-Aspect Effects in Synthetic Aperture Radar Imagery", *Canadian J. Remote Sensing*, **11,1**, pp.39-50.

WOODING, M. G., ZMUDA, A. D., and ATTEMA, E. "An Overview of SAREX-92 Data Acquisition and Analysis of The Tropical Forest Environment", *SAREX-92 Workshop Proceedings*, ESA Headquarters, Paris, 6-8 December 1993, ESA WPP-76, pp. 41-53.

AHERN, F. J., CAMPBELL, F. H. A., ELIZONDO, C., KUX, H. J. H., NOVO, E., PARADELLA, W., RANEY, R. K., SALCEDO, R., SHIMABUKURO, Y., and SINGHROY, V. "C-band SAR for Resource Management in Tropical Environments: Lessons from SAREX-92 Investigations in Brazil, Costa Rica, Venezuela, and Guyana", *SAREX-92 Workshop Proceedings*, ESA Headquarters, Paris, 6-8 December 1993, ESA WPP-76, pp. 41-53.

GUINDON, B. and ADAIR, M. 1992- Analytic formulation of SAR airborne image geocoding 'value-added' and product generation procedure using digital elevation data", *Canadian J. of Remote Sensing*, **18**, pp. 2-11.

HINSE, M., Gwyn, Q. H. and Bonn, F., 1988. "Radiometric correction of C-band imagery for topographic effects in regions of moderate relief", *IEEE Trans. Geosci. Remote Sensing*, **26**, pp122-132.

PCI 1992. - SARSIM1, SARSIM2 SAR Simulation. *Radar Analysis Package Technical Reference*, EASI-PACE version 5.2, pp. 47-53.

EARTHVIEW 1993. SIMSAR SAR Simulation. *EarthView SAR Application Module*. User's Guide and Reference Manual. EarthView Version 4.0, pp. 114-115.

HAWKINS, R. K. , and TEANY, L. D. , 1994. "SAREX 1992 Data Calibration", *SAREX-92 Workshop Proceedings*, ESA Headquarters, Paris, 6-8 December 1993, ESA WPP-76, pp. 41-53.

LAUR, H. 1992. "Derivation of Backscattering Coefficient σ^0 in ERS-1.SAR.PRI Produts". *ERS-1 SAR Calibration*, ESA/ESRIN report. October 17th, 16 p.

WIVELL, C. E., STEINWand D. R., KELLY, G. G., and MEYER, D. J., 1992. "Evaluation of terrain models for the geocoding and terrain correction of SAR Images", *IEEE transactions on Geoscience and Remote Sensing*, **30(6)**, pp. 1137-1144.

BAYER, T., WINTER, R., and SCHREIER, G., 1991. "Terrain influences in SAR backscatter and attempts to their correction". *IEEE transactions on Geoscience and Remote Sensing*,

29(3), pp. 451-462.

ITTEN, K. I., and MEYER, P., 1993. "Geometric and Radiometric Correction of TM data of mountainous Forested Areas". *IEEE Transactions on Geoscience and Remote Sensing*, **31(4)**, pp. 764-770.

TOUTIN, T., CARBONNEAU, Y. and St-LAURENT L., 1992. "An integrated method to rectify airborne radar imagery using DEM", *Photogrammetric Engineering and Remote Sensing*, **58(4)**,p417-422.

ELACHI, C., 1987 "Spaceborn Radar Remote Sensing: Applications and Techniques", *IEEE Press*, New York, p.12.

ULABY, F. T. and DOBSON, M. C., 1989. "Handbook of Radar Scattering Statistics for Terrain", *Artech House*, pp.17-18.

FIGURE CAPTIONS

Figure 1: the synthetic image of the slant range SLR(x,y) (figure 1c), is georeferenced (figure 1d) with the same parameters than the ones used to georeference the radar image (figure 1a and 1b).

Figure 2: Geometry of the airborne (constant alitude ALTI) side looking radar. (a) Constant azimuth plane; (b) constant range plane; (c) top view.

Figure 3: Calculated images of θ_i, θ_r, and θ_a, respectively the incidence angle with respect to the vertical (Equation 1), the local incidence angle in the range direction (Equation 2) and in the local incidence angle in the azimuth direction (Equation 4).

Figure 4: Graph of $\left(\frac{\cos^2(\theta_r)}{\sin(\theta_r)}\right)^{1/2}, (\cos(\theta_a))^{1/2}$ and $\left(\frac{\cos^2(\theta_r)}{\sin(\theta_r)}\right)^{-1/2}, (\cos(\theta_a))^{-1/2}$ showing the dependence on the DN_i and inverse of DN_i on the local incidence angle in the range and azimuth direction (see Equation 7).

Figure 5: HIgh-resolution C-SAR georeferenced subset of the Juan Vinas area, Costa Rica: (a) raw stage (HH = Red, VV = Cyan); (b) radiometrically corrected for the topography using Equation 9, with $H_{ref} = 0$. Speckle has been removed with filtering with a Crimmins geometrical filter. Linear LUTs has been applied for this impression to allow better visual quality while preserving the radiometry.

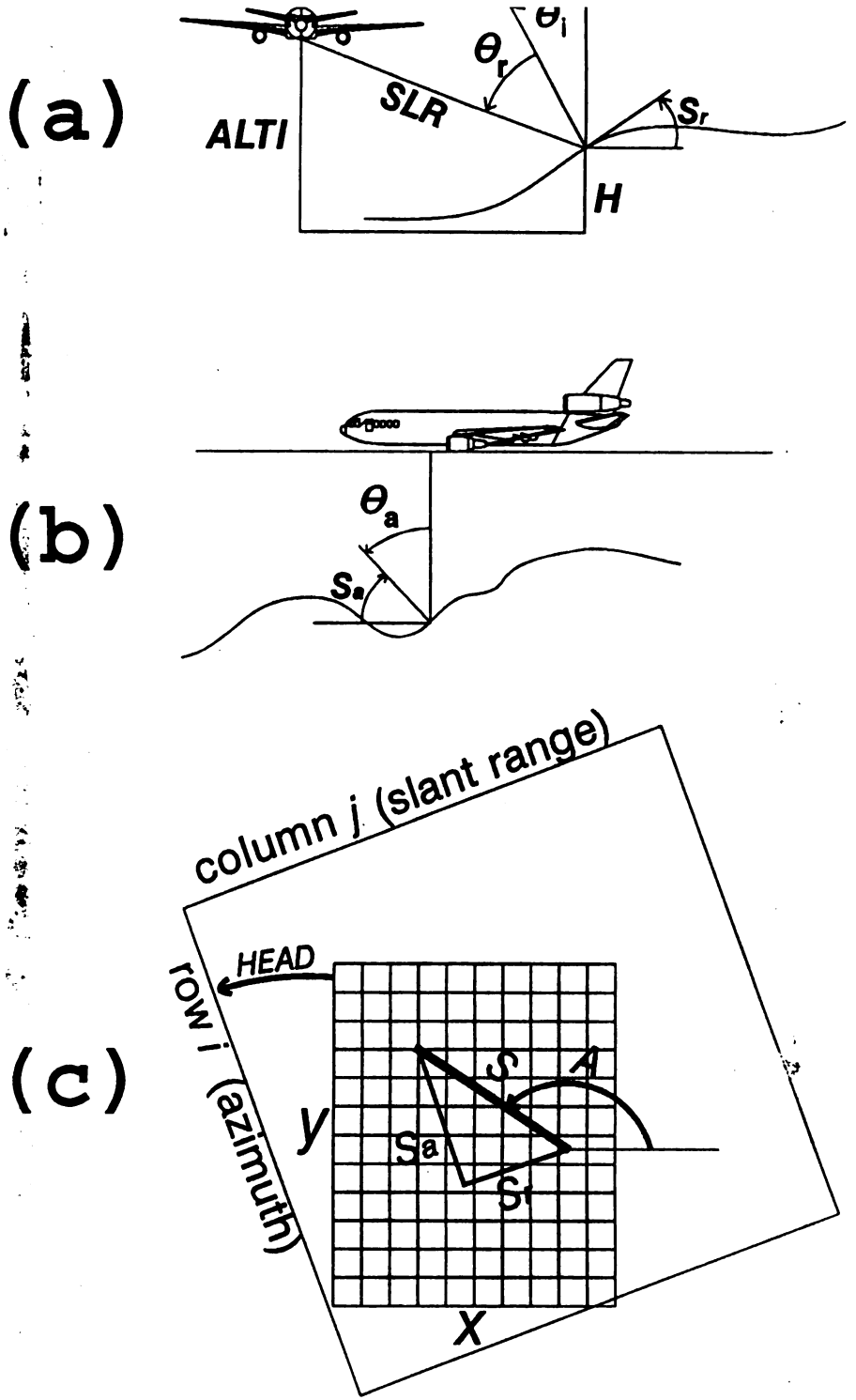
(a)
ALTI
SLR
θ_r
θ_i
S_r
H
(b)
θ_a
S_a
(c)
column j (slant range)
HEAD
row i (azimuth)
y
S_r
A
S_a
S_i
X

figure 1

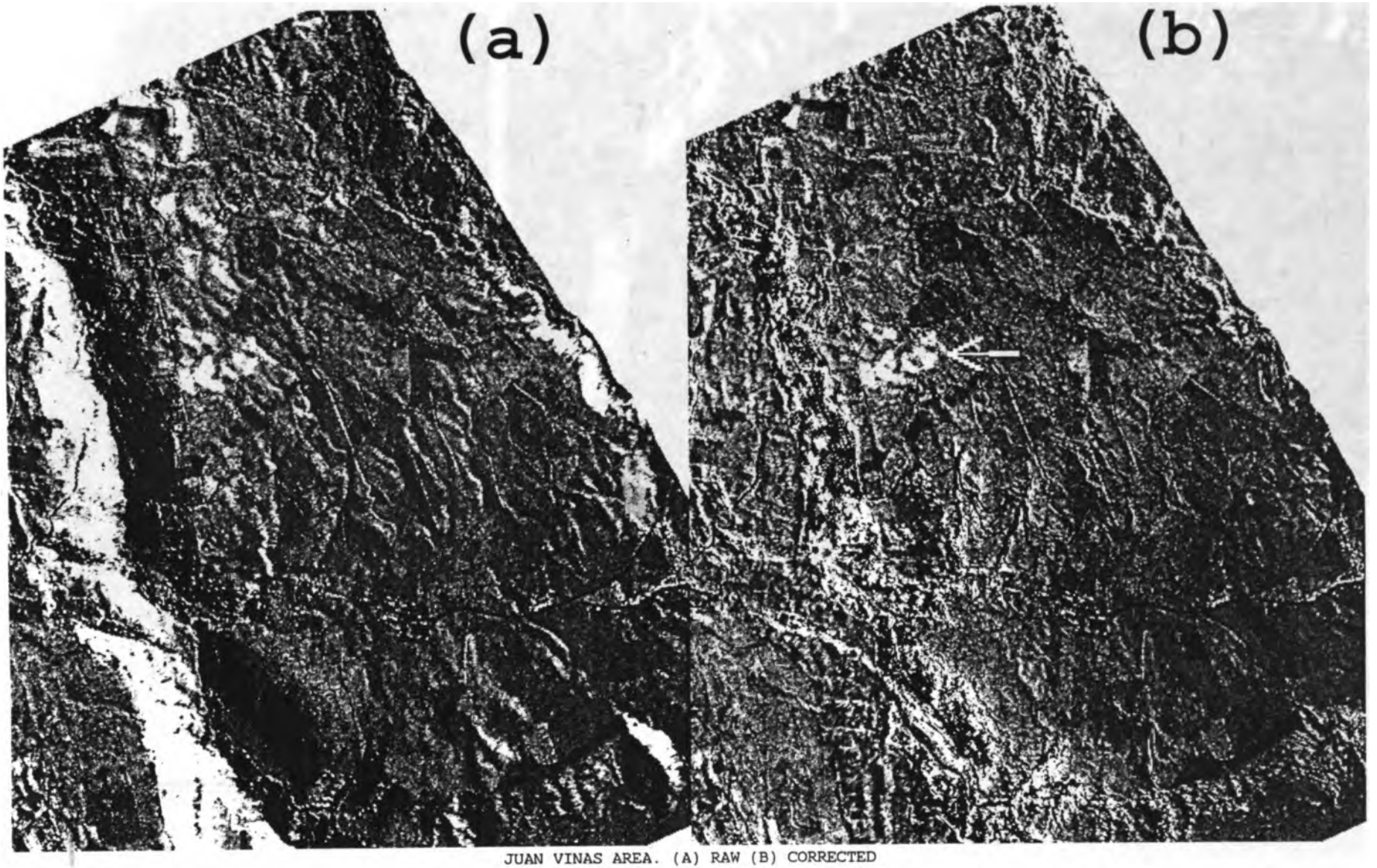

JUAN VINAS AREA. (A) RAW (B) CORRECTED

figure 2

Figure 3

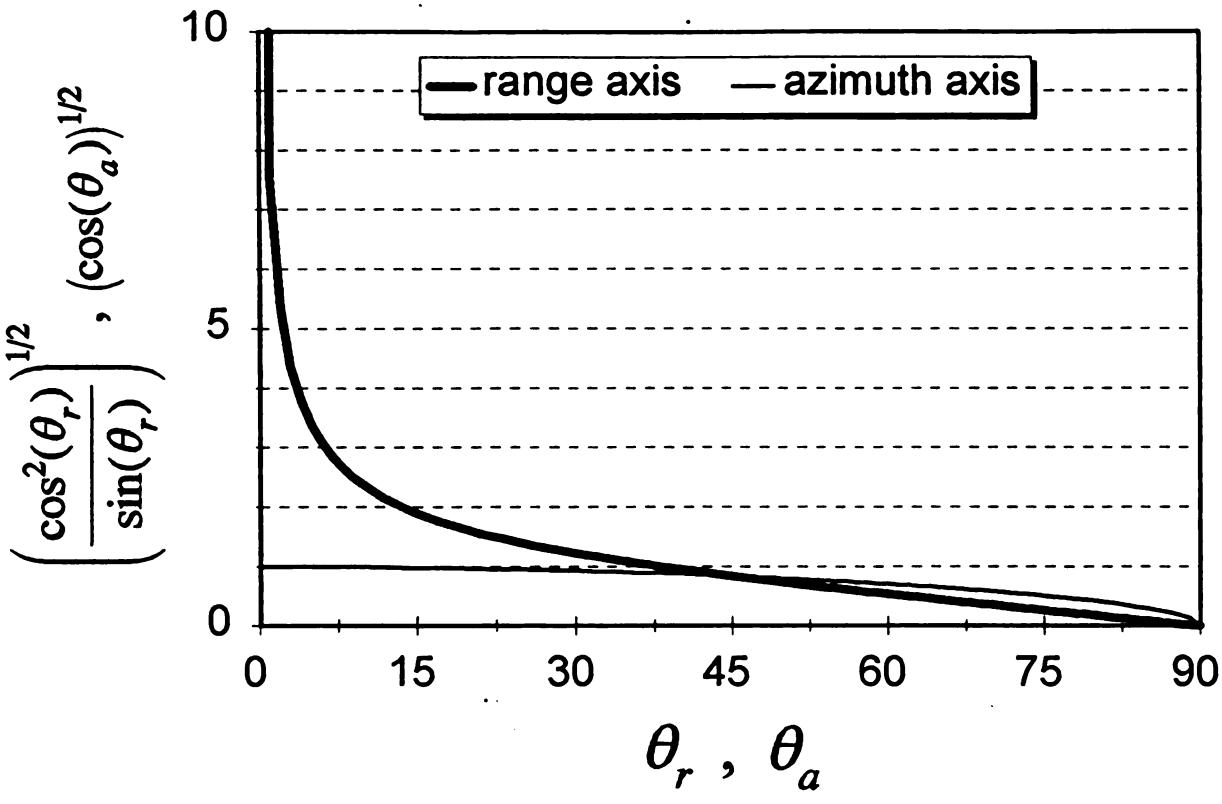
10
5
0
range axis
azimuth axis
0
15
30
45
60
75
90
θ_r , θ_a
$\left(\frac{\cos^2(\theta_r)}{\sin(\theta_r)}\right)^{1/2}$, $(\cos(\theta_a))^{1/2}$

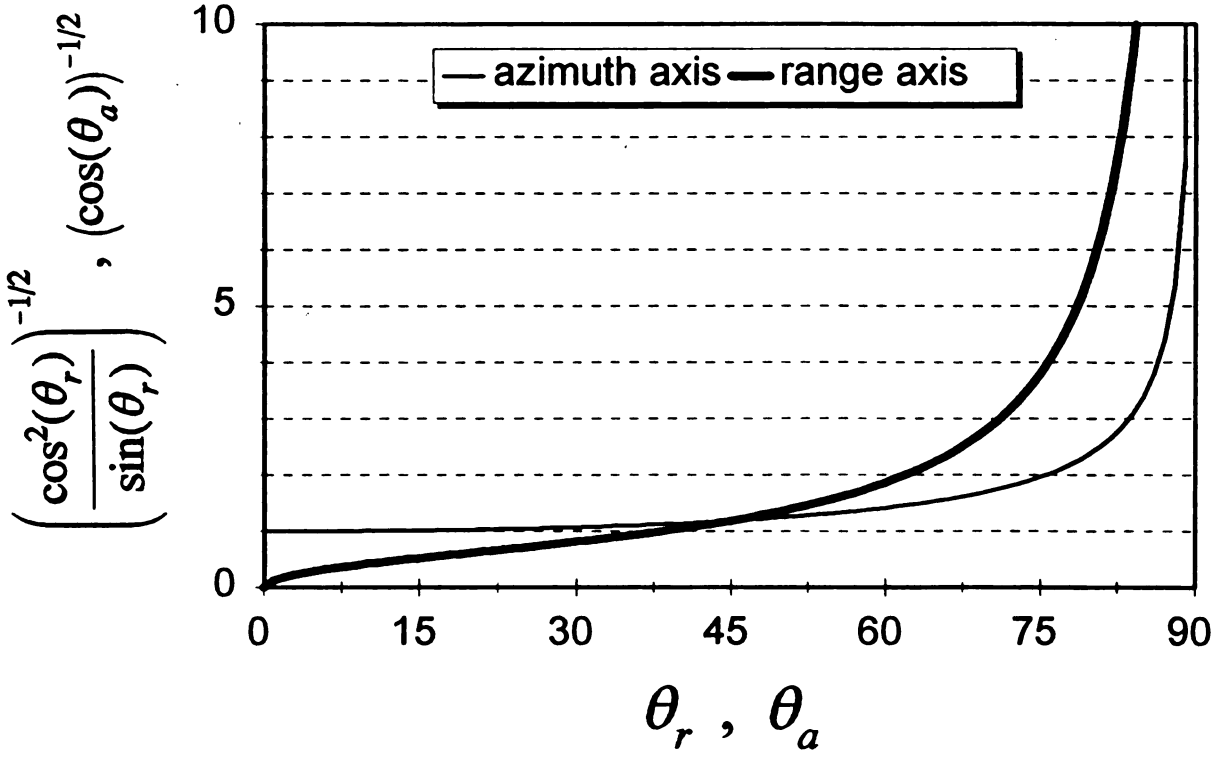
10
5
0
azimuth axis
range axis
0
15
30
45
60
75
90
θ_r , θ_a
$\left(\frac{\cos^2(\theta_r)}{\sin(\theta_r)}\right)^{-1/2}$, $(\cos(\theta_a))^{-1/2}$

figure 4

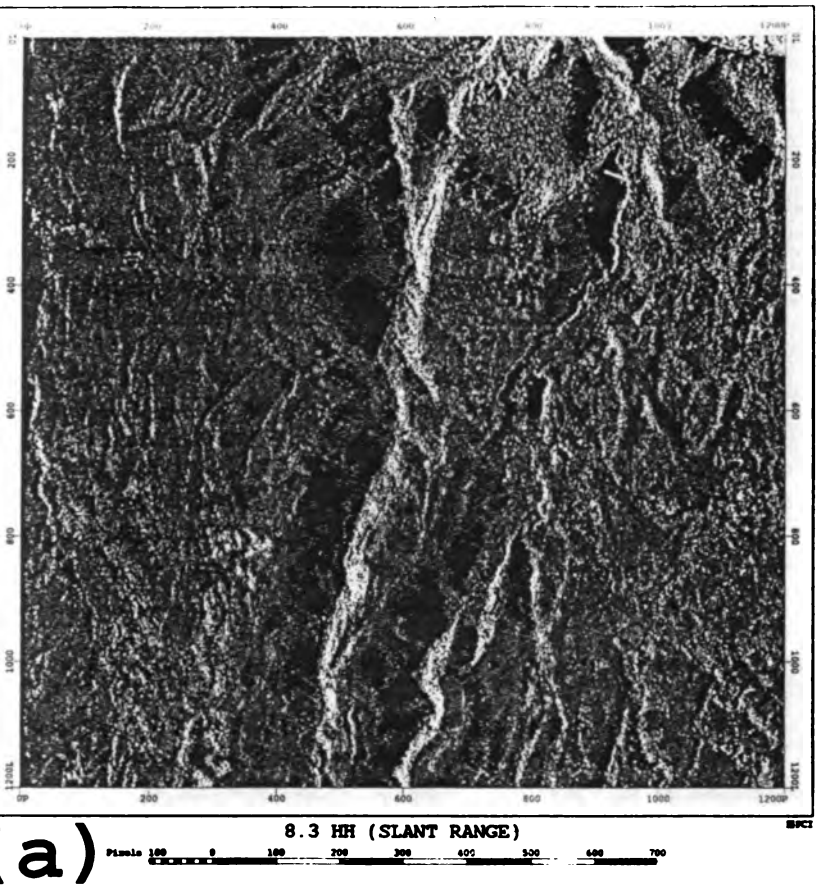

(a)

(b)

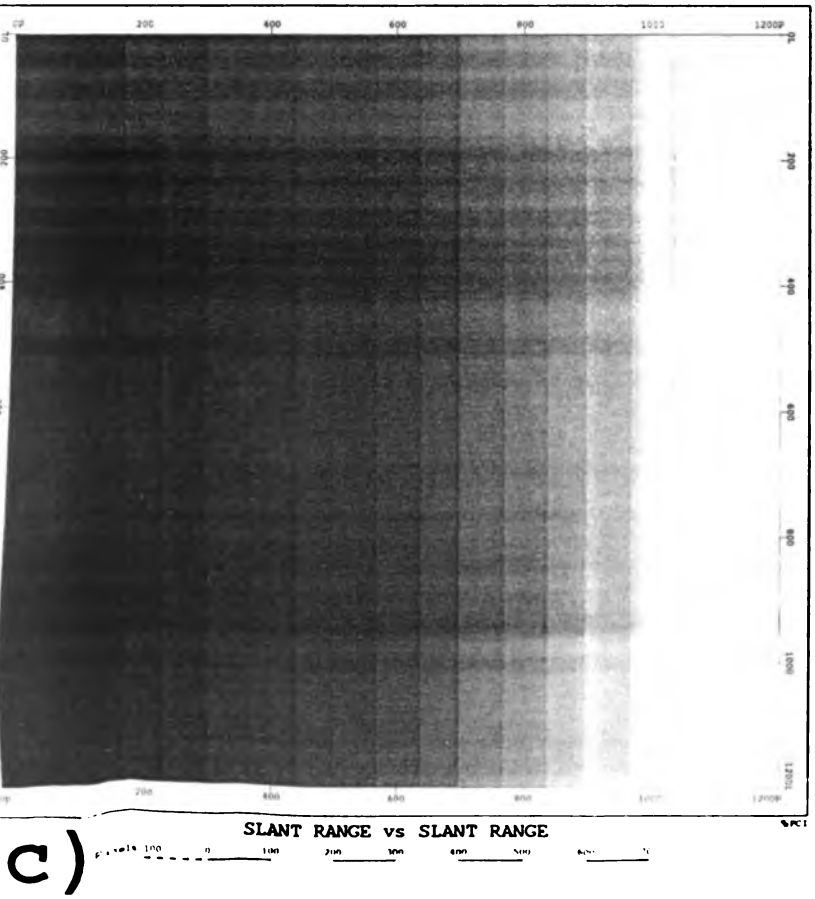

(c)

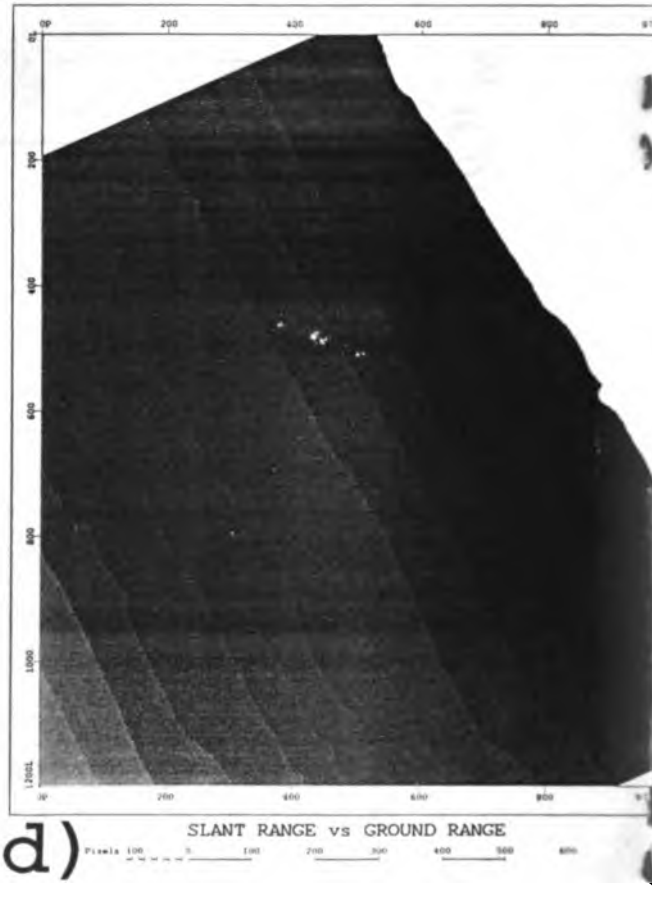

(d)

figure 5